



# Ultrastable and high-performance seawater-based photoelectrolysis system for solar hydrogen generation

Rui-Ting Gao<sup>a</sup>, Xiaotian Guo<sup>a</sup>, Shujie Liu<sup>a</sup>, Xueyuan Zhang<sup>b</sup>, Xianhu Liu<sup>c</sup>, Yiguo Su<sup>a,\*</sup>, Lei Wang<sup>a,\*</sup>

<sup>a</sup> School of Chemistry and Chemical Engineering & Inner Mongolia Engineering and Technology Research Center for Catalytic Conversion and Utilization of Carbon Resource Molecules, Inner Mongolia University, 235 West University Street, Hohhot 010021, China

<sup>b</sup> State Key Laboratory of Chemo/Biosensing and Chemometrics, College of Chemistry and Chemical Engineering, Hunan University, Changsha 410082, China

<sup>c</sup> Key Laboratory of Materials Processing and Mold, Ministry of Education, Zhengzhou University, Zhengzhou 450002, China

## ARTICLE INFO

### Keywords:

High-stability seawater photoelectrolysis  
MoO<sub>3</sub> barrier layer  
(photo)Corrosion resistance  
Surface doping engineering  
Charge transfer

## ABSTRACT

Solar hydrogen production from seawater, the most natural resource on the earth, is an economically appealing for renewable energy conversion. A photoelectrochemical (PEC) seawater-splitting system is greatly challenging for designing stable photoelectrodes and obtaining high and stable photocurrents, strongly preventing corrosion of semiconductors in seawater. In this context, we for the first time report an ultra-stable seawater splitting PEC cell based on the BiVO<sub>4</sub> protected by a MoO<sub>3</sub> barrier layer. The combination of MoO<sub>3</sub> and Mo/B co-doping on BiVO<sub>4</sub> photoanode presents a resembled photocurrent density value of 4.30 mA cm<sup>-2</sup> at 1.23 V<sub>RHE</sub> in simulated seawater and natural seawater under 1 sun AM 1.5G illumination. Equally importantly, the resulting photoanode is quite stable during natural seawater splitting, which shows strong photocorrosion resistance over 70 h of continuous irradiation. Further theoretical calculations provide an insight into the roles of surface dopants for the reduction of substantial surface charge recombination and improving the photocorrosion resistance during long-term operation in the marine environment. This work provides a new avenue for the robust and stable PEC semiconductors design for hydrogen production by seawater photoelectrolysis.

**Broader context:** Seawater photoelectrolysis is one of the promising alternatives for hydrogen production since sun and seawater represent the two most abundant and available resources reserved on earth. However, the corrosion resistance on photoelectrodes should be paid more attention to long-term operation, where the chloride ions from seawater corrode the electrodes. The highly robust and efficient photoelectrodes are thereby required as one of the critical points on potential application. The BiVO<sub>4</sub> photoelectrode is a promising semiconductor for photoelectrochemical (PEC) seawater splitting with a suitable bandgap and favorable conduction band edge position. Unfortunately, this photoelectrode undergoes a poor charge carrier and serious photocorrosion which restricts practical applications for solar energy conversion. In this context, we develop a robust BiVO<sub>4</sub> protected with a MoO<sub>3</sub> barrier layer, constructing with surface dual-doping engineering, which serves as an outstanding PEC electrode for natural seawater photoelectrolysis. We further demonstrate that the optimized photoelectrode presents a resembled photocurrent density value in simulated seawater and natural seawater under 1 sun AM 1.5G illumination, which shows a strong photocorrosion resistance over 70 h of continuous irradiation, representing one of the targets directly avoiding chloride corrosion on seawater photoelectrolysis.

## 1. Introduction

Recently, large-scale and sustainable hydrogen production from seawater is becoming a promising alternative to solar-to-hydrogen conversion since sun and seawater represent the two most abundant

and available resources reserved on earth [1–6]. Distinct from the fresh water, seawater has large amounts of chloride ions (Cl<sup>-</sup>), which are easily oxidized than H<sub>2</sub>O oxidation owing to the lower overpotential. The oxygen evolution reaction (OER) and chlorine evolution reaction (CER) become the competitive reaction at the photoanode due to their very

\* Corresponding authors at: School of Chemistry and Chemical Engineering & Inner Mongolia Engineering and Technology Research Center for Catalytic Conversion and Utilization of Carbon Resource Molecules, Inner Mongolia University, China.

E-mail addresses: [cesyg@imu.edu.cn](mailto:cesyg@imu.edu.cn) (Y. Su), [wanglei@imu.edu.cn](mailto:wanglei@imu.edu.cn) (L. Wang).

<https://doi.org/10.1016/j.apcatb.2021.120883>

Received 29 September 2021; Received in revised form 27 October 2021; Accepted 30 October 2021

Available online 21 November 2021

0926-3373/© 2021 Elsevier B.V. All rights reserved.

close thermodynamic potentials [7–13]. Meanwhile, the poor stability of photoanode principally prevents the continuous hydrogen generation at the cathode in seawater cells. A seawater splitting photoelectrochemical (PEC) system is greatly challengeable for designing robust photoelectrodes and obtaining high and stable photocurrents, strongly preventing corrosion of semiconductors.

Alternatively,  $\text{Cl}_2$  is an important product in the industrial chlor-alkaline process and even some industries prefer  $\text{Cl}_2$  production for wastewater treatment, and therefore it is desirable this by-product in sustainable energy application [4,14,15]. Since 2011, Zou and Li et al. [16] started research on Mo doped  $\text{BiVO}_4$  photoanode for solar hydrogen generation from seawater. The modified photoanode exhibited a photocurrent density of  $2.16 \text{ mA cm}^{-2}$  at  $1.0 V_{\text{RHE}}$  in natural seawater under AM 1.5G sunlight (1 sun), which was assigned to the improved conductivity and the increased hole diffusion length by Mo doping. Besides, the cheap and effective oxygen evolution catalysts are demanded to promote the practical application on solar hydrogen production. After that, the research on seawater-based photoelectrolysis is seldom reported. As for one of the critical points on potential application, the corrosion resistance in seawater photoelectrolysis for long-term operation should be paid more attention, since some non-innocuous ions and particulates may poison the photoelectrodes.

Herein, in this work, the synergism of the molybdenum trioxide ( $\text{MoO}_3$ ) layer and the Mo/B codoping on  $\text{BiVO}_4$  semiconductors (noted as MoB/BVO) was proposed to address the aforementioned issues, for improving PEC seawater splitting performance and photocorrosion resistance. The cathode potentiostatic polarization measurement was employed to form the defect-induced  $\text{MoO}_3$  ( $\text{MoO}_{3-x}$ ) with mixed  $\text{Mo}^{6+}/\text{Mo}^{5+}$  oxidation states, and in the meanwhile, dual Mo and B were doped on the surface of  $\text{BiVO}_4$ , beneficial for the increased surface conductivity. The high work function (6.6 eV) and hole-transport properties of  $\text{MoO}_{3-x}$  make solar-energy-conversion efficiency markedly stable in the PEC seawater system. The doped Mo and B without catalyst modification provide a passivator on reducing the surface charge recombination for facilitating fast seawater splitting. The MoB/ $\text{BiVO}_4$  photoanode presents a resembled photocurrent density value of  $4.30 \text{ mA cm}^{-2}$  at  $1.23 V_{\text{RHE}}$  in simulated seawater and natural seawater systems under one sun AM 1.5 G illumination. Notably, a durable photoanode can be achieved, which exhibits a long-term stability over 70 h of illumination in natural seawater. The theoretical calculations further provide an understanding the roles of surface dopants in promoting seawater photoelectrolysis. This work has demonstrated an ultra-stable PEC cell with highly efficient and stable performance for seawater splitting, which surpasses the previously reported results.

## 2. Experimental

### 2.1. Preparation of $\text{BiVO}_4$ , B/ $\text{BiVO}_4$ , Mo/ $\text{BiVO}_4$ , MoB/ $\text{BiVO}_4$

$\text{BiOI}$  was prepared according to the previously reported method [17–19]. 100 mL KI (0.4 M) was added into 0.04 M  $\text{Bi}(\text{NO}_3)_3 \cdot 5\text{H}_2\text{O}$ , in which  $\text{HNO}_3$  was added to adjust the pH value to 1.7. The solution was mixed with a 40 mL ethanol solution containing 0.23 M p-benzoquinone. The deposition was performed at  $-0.1 V_{\text{Ag}/\text{AgCl}}$  for 300 s to form  $\text{BiOI}$ . The dimethyl sulfoxide (DMSO) solution containing 0.2 M vanadyl acetylacetonate ( $\text{VO}(\text{acac})_2$ ) was dropped on the top surface of  $\text{BiOI}$ . The initial  $\text{BiOI}$  with the above solution was annealed at  $450^\circ\text{C}$  for 2 h in air condition. Then, the annealed  $\text{BiVO}_4$  (noted as BVO) was immersed in 1 M NaOH for 30 min to get rid of excess  $\text{V}_2\text{O}_5$ .

To prepare the MoB/BVO, the BVO was electrodeposited at a potential of  $0.3 V_{\text{RHE}}$  for a certain time (3 h, 6 h, and 12 h) in 1 M potassium borate (KBI) aqueous solution containing various concentrations (0.1 mM, 0.5 mM, 5 mM, and 10 mM) of ammonium molybdate in dark. The electrodeposition time and the concentration of ammonium molybdate were optimized in this process. Similar preparation approach was used on the preparation of Mo/ $\text{BiVO}_4$  or B/BVO in the precursor of

ammonium molybdate or KBI.

### 2.2. Photoelectrochemical measurements

Photoelectrochemical measurements were conducted in a standard three-electrode system with an electrochemical analyzer (CHI760D, CH Instruments, Inc.). The light source was simulated sunlight AM 1.5G ( $100 \text{ mW cm}^{-2}$ , PLS-FX300HU, Beijing Perfectlight Technology Co., Ltd.). All samples were illuminated from front side. Simulated seawater (SSW) and natural seawater (SW) were used as the electrolyte. The SSW was prepared by the chemicals (NaCl, 27.21 g;  $\text{MgCl}_2$ , 3.81 g;  $\text{MgSO}_4$ , 1.66 g;  $\text{CaSO}_4$ , 1.404 g;  $\text{K}_2\text{SO}_4$ , 0.577 g;  $\text{K}_2\text{CO}_3$ , 0.2124 g;  $\text{MgBr}_2$ , 0.08 g) dissolved in 1 L distilled water. The pH value of SSW was 8.0. The SW was obtained from Huanghai, Shandong, Province China. The pH value of SW was 7.8. Photocurrent vs. voltage ( $I$ - $V$ ) curves were recorded by scanning the potential from  $-0.5$  to  $0.8 V_{\text{Ag}/\text{AgCl}}$  with a rate of  $10 \text{ mV s}^{-1}$ . The measured potential was converted into a potential with respect to a reversible hydrogen electrode (RHE). Incident light-electron conversion efficiency (IPCE) was measured at  $1.23 V_{\text{RHE}}$  in simulated sea water using Xe lamp. Electrochemical impedance spectroscopy (EIS) was performed at  $1.23 V_{\text{RHE}}$ , and a small AC amplitude of 10 mV in the frequency range of  $10^2$ - $10^5$  Hz under AM 1.5G illumination. The charge separation efficiency ( $\eta_{\text{abs}} \times \eta_{\text{sep}}$ ) and surface charge injection efficiency ( $\eta_{\text{surface}}$ ) were measured in SSW with the addition of  $\text{Na}_2\text{SO}_3$ . The cyclic voltammetry (CV) measurement was performed following by the study reported by Hamann et al. [20] The Mo/ $\text{BiVO}_4$  electrode was kept in 0.5 M  $\text{Na}_2\text{SO}_4$  (pH=7) applied at  $2.0 V_{\text{Ag}/\text{AgCl}}$  for 120 s to completely oxidize under light. Next, the CV test was performed at a scanning rate of  $2 \text{ V s}^{-1}$  in dark. For the long-term durability, the tested samples were carried out at  $1.23 V_{\text{RHE}}$  in SSW and SW, respectively.

### 2.3. Chlorine determination by o-tolidine

Chlorine gas is soluble in water ( $3.26 \text{ g L}^{-1}$  at  $25^\circ\text{C}$ ), and can react with water to form hydrochloric acid (HCl) and hypochlorous acid (HClO), according to formula ( $\text{Cl}_2 + \text{H}_2\text{O} \rightleftharpoons \text{HClO} + \text{HCl}$ ). To further determine the reaction rate of the anode reaction, an o-tolidine test was performed to quantify the amount of  $\text{Cl}_2$  formed. Since HClO quickly balances with  $\text{Cl}_2$  and  $\text{H}_2\text{O}$ , it could not be separated from the aqueous solution. Therefore, the redox reaction between HClO and o-tolidine produced by the process of seawater splitting was used to determine the  $\text{Cl}_2$  content in the electrolyte. The test solution contained 10 mL distilled water and 0.5 mL o-tolidine solution. To obtain a calibration curve, 1 g  $\text{KMnO}_4$  and 10 mL concentrated HCl were mixed in a sealed bottle for 15 mins to generate  $\text{Cl}_2$ . Use plunger needle syringes to collect different amounts of freshly generated  $\text{Cl}_2$  (1, 2.5, 5, 10, and 20  $\mu\text{L}$ ) and inject the test solution. The seawater decomposition experiment was carried out in 20 mL SSW electrolyte. Under the applied potential of  $1.23 V_{\text{RHE}}$ , 0.1 mL of electrolyte solution was collected at different times, added to the color-developing solution, placed for 10 mins, and then put into the UV-Visible spectrum for testing.

### 2.4. Materials characterization

The crystalline structure was identified by X-ray diffraction analysis (XRD, Rigaku RINT-2000) using  $\text{Cu K}\alpha$  radiation at 40 kV and 40 mA. The elemental composition was determined by X-ray photoelectron spectroscopy (XPS, ESCALAB 250xi, Thermo Fisher Scientific). Scanning electron microscopy (SEM) and transmission electron microscopy (TEM) were performed using FE-SEM/Supra 55 (Zeiss, Germany) and JEM-2100 F (JEOL, Japan) systems. UV-Visible diffuse reflectance spectra were performed on a UV-2600 (Shimadzu) spectrometer by using  $\text{BaSO}_4$  as the reference. The electron paramagnetic resonance (EPR) measurements were recorded using a JES-FA200 spectrometer at low temperature ( $-150^\circ\text{C}$ ).

## 2.5. DFT calculation

Spin-polarized DFT calculations were performed with periodic supercells under the generalized gradient approximation (GGA) using the Perdew-Burke-Ernzerhof (PBE) functional for exchange-correlation and the ultrasoft pseudopotentials for nuclei and core electrons. The Kohn-Sham orbitals were expanded in a plane-wave basis set with a kinetic energy cutoff of 50 Ry and the charge-density cutoff of 700 Ry. The Fermi-surface effects had been treated by the smearing technique of Methfessel and Paxton, using a smearing parameter of 0.02 Ry. The convergence criteria were set as  $10^{-3}$  Ry/Bohr of Cartesian force components acting on each atom and  $10^{-5}$  Ry of total energy.  $\text{BiVO}_4$  (-111) surface with supercell of  $2 \times 2$  was cleaved as the study surface. Mo/BVO and B/BVO were modelled by replacing the V in the first layer, and for MoB/BVO, the Mo and B both take half of the replacement of 1st layered V. The surface oxidation state was checked based on the method given in ref [21]. During the optimization, only the bottom layer remains fixed. The Brillouin-zones were sampled with a  $2 \times 2 \times 1$  k-point mesh. The PWSCF codes contained in the Quantum ESPRESSO [22] distribution was used to implement the calculations.

## 3. Results and discussion

### 3.1. Seawater-based PEC performance enhancement

The BVO photoanodes were synthesized based on the previously reported approach [17–19]. With the purpose of deposition of  $\text{MoO}_3$  layer on the top surface, the BVO was potentiostatically polarized at 0.3  $V_{\text{RHE}}$  for 6 h with a current density of  $\sim 0 \text{ mA cm}^{-2}$  in 1 M borate buffer (KBI) solution containing 0.5 mM ammonium molybdate ( $(\text{NH}_4)_2\text{MoO}_4$ ) as depicted in Fig. S1, following with the thermal treatment in Ar atmosphere at 400 °C for 1 h. The treated sample was marked as MoB/BVO. The Mo/BVO or B/BVO sample was subsequently prepared in the same condition without B or Mo in precursor as a point of comparison. The photoelectrochemical seawater splitting performances for the corresponding samples were evaluated in simulated seawater (SSW)

under one sun AM 1.5 G front illumination. As observed from Fig. 1a, the pristine BVO exhibits a photocurrent of  $1.45 \text{ mA cm}^{-2}$  at 1.23  $V_{\text{RHE}}$  with an onset potential of 0.5  $V_{\text{RHE}}$  in seawater medium. After the modification of Mo or B, the photocurrent densities of Mo/BVO and B/BVO electrodes raise to  $2.70 \text{ mA cm}^{-2}$  and  $3.75 \text{ mA cm}^{-2}$  at 1.23  $V_{\text{RHE}}$ , respectively. Further decoration of MoB displays the maximum photocurrent density of  $4.3 \text{ mA cm}^{-2}$  at the same potential, which is 3 times higher than that of the untreated BVO. The onset potential is negatively shifted by 100 mV (0.4  $V_{\text{RHE}}$ ) compared to the BVO. Various electro-deposition times and  $(\text{NH}_4)_2\text{MoO}_4$  concentrations in KBI were considered in detail on the optimum modulation assignment of  $\text{MoO}_3$  layer under front or back illumination (Fig. S2). It is definitely assured that the front-illuminated PEC performances are better than those of back-side irradiation under the optimum condition, consistent with the previous report on Mo doped  $\text{BiVO}_4$  [16]. Further, there is no obvious variation under back-side illumination regarding deposition time or  $(\text{NH}_4)_2\text{MoO}_4$  concentration (Fig. S2b,d). Fig. 1b shows the transient photoresponses of the electrodes applied at 1.23  $V_{\text{RHE}}$  in SSW condition. The surface recombination is significantly reduced,  $i/i_0$  closed to 1, on the Mo/BVO and MoB/BVO electrodes. This suggests that no charge accumulation is found for these electrodes, and the Mo and MoB modification could accelerate the catalytic rate of seawater splitting. Moreover, the MoB/BVO in electrochemical impedance spectroscopy (EIS) (Fig. 1c) presents the lowest interfacial charge transfer resistance ( $R_{\text{ct}}$ , 94.84  $\Omega$ ) among these electrodes (Table S1). The enhanced PEC performance can be confirmed by incident photon-to-current efficiency (IPCE) measurement further, in which the MoB/BVO has excellent IPCE value, with 70% approximately at 350–400 nm (Fig. 1d). The band gaps of BVO and B/BVO electrodes as calculated from the evaluation of an indirect band gap ( $E_g$ ), i.e., as  $(\text{IPCE} \times h\nu)^{1/2}$  versus photon-energy ( $h\nu$ ), exhibit the values of 2.43 and 2.42 eV; after the deposition of Mo and MoB, the resulting  $E_g$  is shifted to 2.40 eV, which is slightly lower than the pristine BVO (Fig. 1e), denoting the change in the material structure. The UV-Vis spectra of all the samples as evident in Fig. 1f show the difference in the light absorption, - the tail absorption at 500–800 nm detected on the Mo/BVO, B/BVO, and MoB/BVO. We therefore assume that the

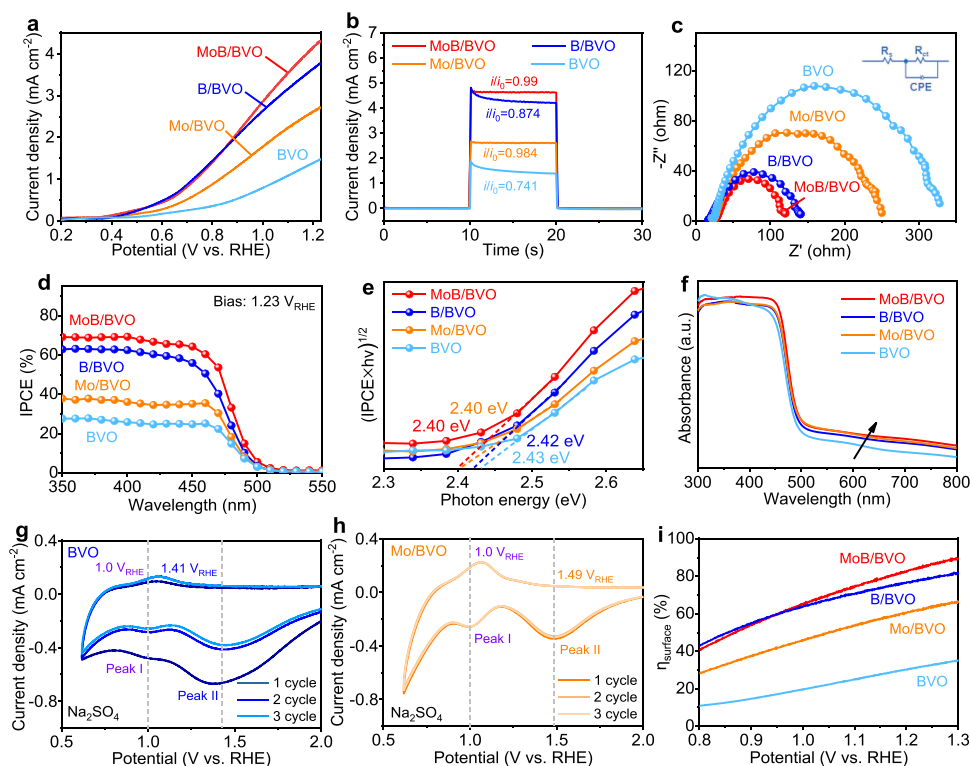


**Fig. 1.** PEC characterization of BVO, B/BVO, Mo/BVO, and MoB/BVO: (a) J-V curves in SSW (pH=8) under AM 1.5 G (100  $\text{mW cm}^{-2}$ ) front-side illumination; (b) transient photoresponse; (c) EIS under AM 1.5 G illumination; (d) IPCE values; (e) band gaps of BVO, B/BVO, Mo/BVO, and MoB/BVO determined from photocurrent measurements; (f) UV-Vis spectra; (g,h) cyclic voltammetry of (f) BVO and (g) Mo/BVO in  $\text{Na}_2\text{SO}_4$  in the dark; Inset of c shows the equivalent circuit model; (h) surface separation efficiencies of BVO, B/BVO, Mo/BVO, and MoB/BVO.



generated oxygen vacancies ( $O_v$ ), and Mo or B doped into the surface of BVO during the electrodeposition used in this case may be one of the main effects for boosting PEC performance. Meanwhile, the enhancement of the front-illuminated PEC performance of MoB/BVO electrode could be ascribed to the better light utilization as confirmed by Fig. 1f and inset of Fig. S1.

In an effort to find the underlying mechanism on the charge carrier migration involved in  $MoO_3$ , the cyclic voltammetry (CV) measurements were performed on BVO and Mo/BVO in  $Na_2SO_4$  in dark to explain the completed surface oxidation state. As shown in Fig. 1g and h, the cathode scanning in the first cycle represents the charge carrier recombination in the conduction band. Two inherent redox reactions are observed: at  $1.0 V_{RHE}$  (peak I) the reversible transition process attributable to  $V^{4+}/V^{5+}$ , which is related to the electron capture process at the charge transfer site;  $1.41 V_{RHE}$  (peak II) is the irreversible process of  $VO_2^+$  representing a reduction of bismuth vanadate to  $VO^{2+}$ , which is associated with the electron capture process of surface recombination. Most of the electrons on the BVO electrode participate in the reduction process of  $VO_2^+$ , which is considered to be the recombination center of surface trapped electrons, resulting in low PEC performance [23,24]. On the contrary, this recombination can be greatly suppressed on the Mo/BVO, where the peak II in the first scanning cycle is remarkably weakened, and moves towards a high potential ( $1.49 V_{RHE}$ ). The surface reaction rate on BVO depends on the number of  $V^{4+}/V^{5+}$ . Interestingly, the intensity of peak I on Mo/BVO is slightly greater than that of BVO, and the observable reversible behavior indicates that the capture and release of charges are very rapid, so this kind of electron trapping would not lead to a large number of charge carrier recombination. The holes extracted from the valence band of BVO migrate rapidly at the interface

of Mo/BVO, which may be caused by the presence of Mo on the surface. This result is also compatible with the intensity weakening of the XRD pattern (Fig. S3) and the negative shift of the Raman spectrum on Mo/BVO (Fig. S4). On the other hand, the  $V^{4+}$  would be formed during the capture process, accompanied by the generated  $O_v$ . The generated  $O_v$  helps to absorb oxygen/hydroxyl substances at the surface, which further improves the hole transfer ability and accelerates the surface reaction kinetics. Besides, the MoB/BVO shows a high surface charge separation efficiency in comparison to the other electrodes (Fig. 1i and S5).

### 3.2. Characterization of photoanodes with surface engineering

Scanning electron microscopy (SEM) and transmission electron microscopy (TEM) were employed to investigate the details of surface structure on the corresponding samples (Fig. 2a-h). The B/BVO sample (Fig. 2 and S6) shows the identical surface morphology with the pristine BVO (Fig. 2a). Viewed from TEM images of Fig. 2e and f, an amorphous layer with a thickness of 1–2 nm is covered on the surface of BVO or B/BVO. Although a similar surface structure is detected on these samples, a notable difference in the PEC performances can be obtained in Fig. 1a. The ultrathin layer on B/BVO is referred to the borate modification, leading to the increased chemisorbed -OH groups from  $[B(OH)_4]^-$  or -OH, which facilitate the surface reaction [25,26]. After the modification of Mo and MoB on BVO (Fig. 2c,d), both surfaces become rough compared to the BVO. The thick and uneven layers are grown on the samples (Fig. 1 and S7,S8). The clear lattice fringes with the distances of 0.309 nm, 0.433 nm, and 0.304 nm correspond to the (112), (111), and (211) planes of  $MoO_3$  (Fig. 2g), confirming the formation of  $MoO_3$

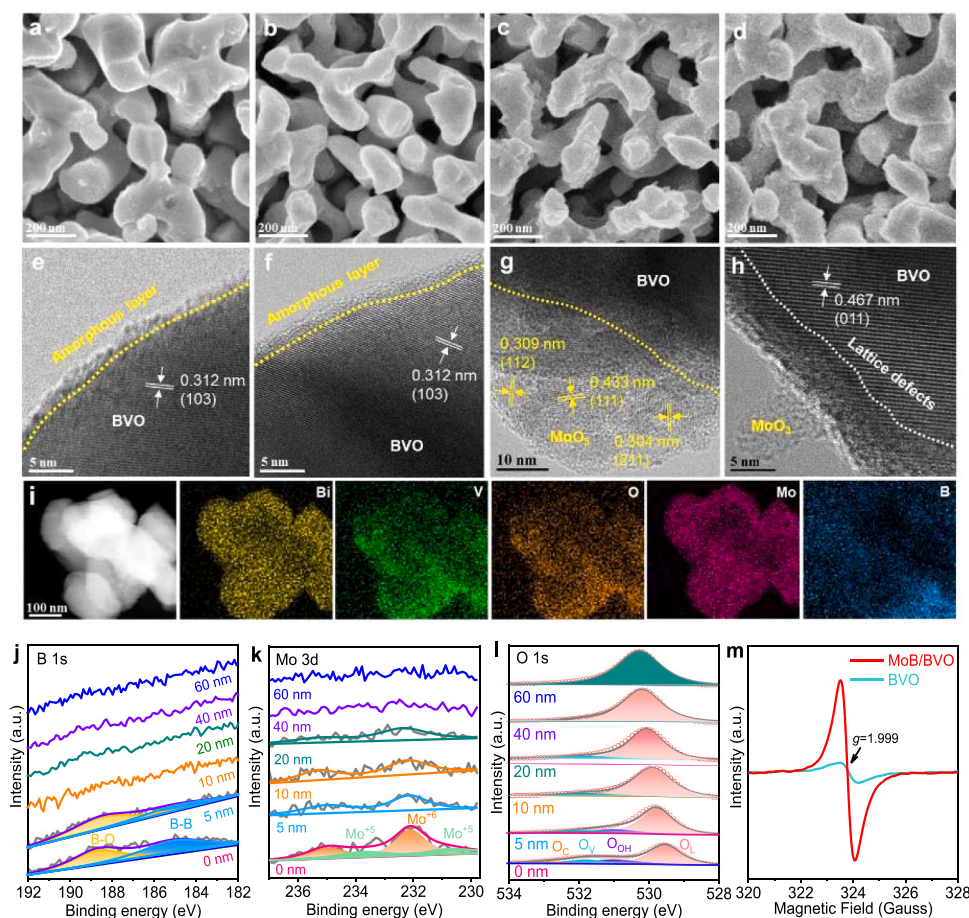


**Fig. 2.** (a-d) SEM images of (a) BVO, (b) B/BVO, (c) Mo/BVO, and (d) MoB/BVO; (e-h) HRTEM images of (e) BVO, (f) B/BVO, (g) Mo/BVO, and (h) MoB/BVO; (i) TEM-EDS elemental mapping of MoB/BVO; (j-l) XPS (j) B 1s, (k) Mo 3d, and (l) O 1s depth profiles of MoB/BVO; (m) EPR spectra of BVO and MoB/BVO.

anchored on the top surface [27,28]. Further detected from MoB/BVO sample, the lattice defect closed to the interface is observed on the BVO side (Fig. 2h), which is assigned to the induced defects on the surface during the cathodic potentiostatical polarization. What's more, the TEM-EDS element mapping (Fig. 2i) displays the signals of Bi, V, O, and Mo, whereas the B element looks not obvious owing to the low content on the surface. Besides, the boron is a very light element, and could not be examined due to the detection limit since it was in a system with heavy metal (e.g., Bi). This phenomenon can also be observed on B modified BiVO<sub>4</sub> sample in Sun et al.'s report [25]. Fortunately, X-ray

photoelectron spectroscopy (XPS) exhibits the typical B 1s signal (Fig. S9d). The Bi 4f, V 2p, and O 1s spectra exhibit negligible shifts on both BVO and B/BVO (Fig. S9a-c). However, the negative shift to high binding energy is detected on the deposition with Mo and MoB, which is ascribed to the presence of MoO<sub>3</sub> on the top surface (Fig. 2g,h). Since the MoO<sub>3</sub> was deposited, it leads to the decreased V content (4.40–5.73 at %) owing to V<sup>5+</sup> replaced by Mo<sup>6+</sup> (Fig. S9f). The TEM-EDS line scan profile again demonstrates this assumption (Fig. S10). As the V is easily dissolved into the electrolyte during long-term operation, the V replaced by Mo may be beneficial to the photocorrosion inhibition.

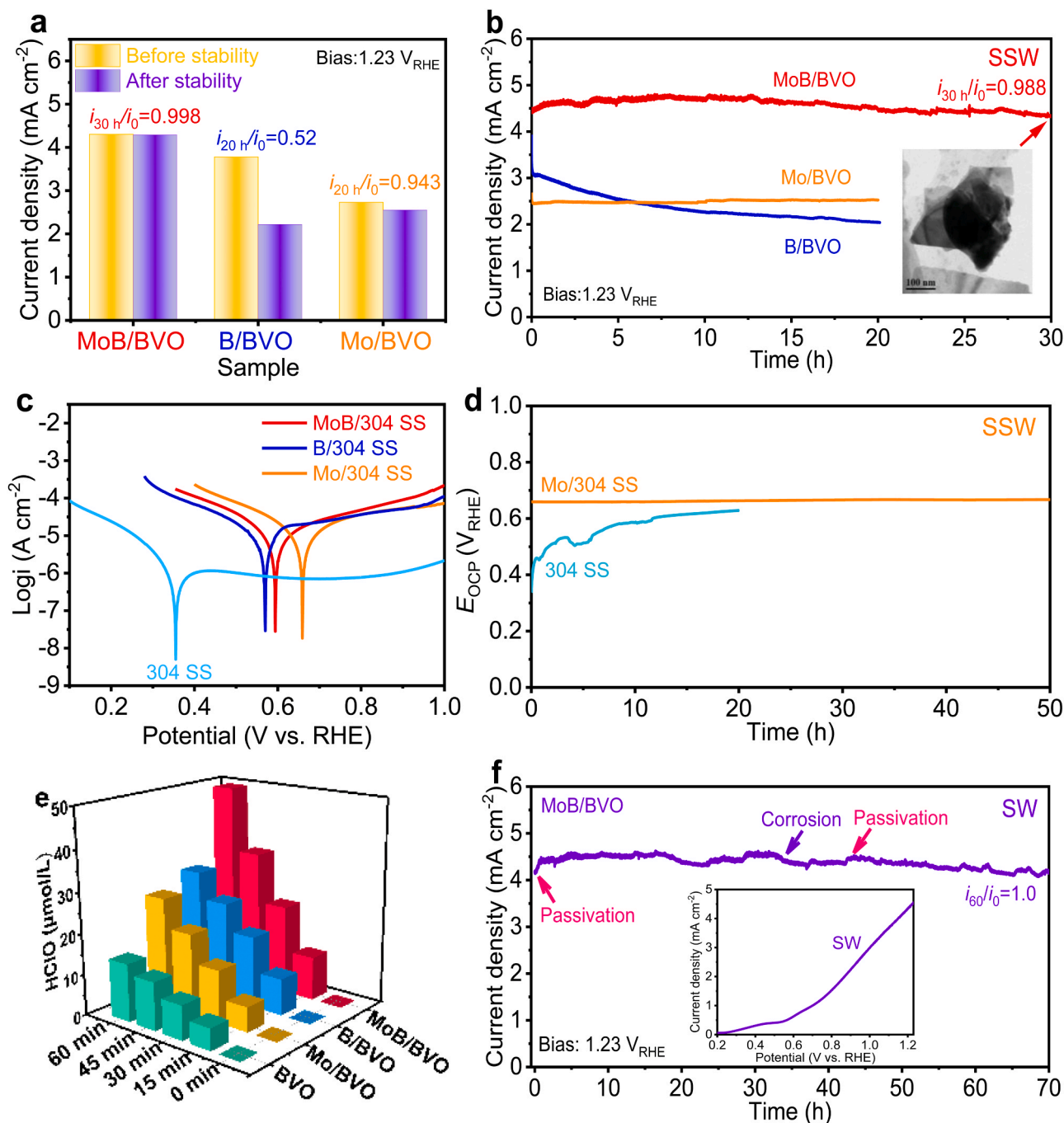


**Fig. 3.** (a) Comparison of photocurrents for B/BVO, Mo/BVO, and MoB/BVO at 1.23 V<sub>RHE</sub> before and after stability; (b) long-term durability of B/BVO, Mo/BVO, and MoB/BVO applied at 1.23 V<sub>RHE</sub> in SSW under AM 1.5G (100 mA cm<sup>-2</sup>) front-side illumination; (c) polarization curves for Mo, B, and MoB grown on 304 stainless steel in SSW; (d) time variation of open circuit potential (OCP) on MoO<sub>3</sub> grown on 304 stainless steel in SSW. The OCP value of 304 stainless steel was shown for comparison; (e) estimated amounts of HClO generated from photoanodes with different systems; (f) long-term durability of MoB/BVO applied at 1.23 V<sub>RHE</sub> in SW under AM 1.5G (100 mA cm<sup>-2</sup>) front-side illumination. Inset shows the J-V curve of electrode in SW under AM 1.5G (100 mA cm<sup>-2</sup>) front-side illumination.

We further performed XPS depth profile measurements to examine the Mo and B contents present on the top surface (Figs. 2j–l and S11). Note that the B is located around 5–10 nm from the top surface (Fig. 2j), whereas Mo is doped into the BVO with a thickness of 20–40 nm and the content of Mo is 2.01–7.28 at% (Fig. 2 and S11c). This could be conferred to the potentiostatical polarization at a low applied potential for a stipulated time, which leads to the formation of defects, making a case for driving charge separation and transport. To further probe the defects existed on the materials, X-band electron paramagnetic resonance (EPR) spectroscopy of MoB/BVO exhibits the strong  $g$  signal intensity compared to the BVO (Fig. 2 and S12), implying the induced defects of potentiostatic polarization on BVO, which coincides with the TEM and XPS observation.

### 3.3. Long-term photocorrosion resistance for photoelectrolysis system

The seawater has large amounts of chloride ions ( $\text{Cl}^-$ ), and long-term durability is one of the essential factors for evaluating the solar seawater splitting performance. Fig. 3a and b show the  $J$ - $t$  curves of Mo/BVO, B/BVO, and MoB/BVO photoanodes in SSW under AM 1.5 G front illumination. The photocurrent densities almost remain,  $i_{20\text{ h}}/i_0 = 0.943$  and  $i_{30\text{ h}}/i_0 = 0.998$ , after testing for 20 h and 30 h on Mo/BVO and MoB/BVO electrodes, respectively. The PEC performance of MoB/BVO after stability is similar to the value at the initial time (Fig. S13). Conversely, the B/BVO electrode has a remarkable decrease in photoresponse ( $i_{20\text{ h}}/i_0 = 0.52$ ), identical with the BVO with a decay for 3 h (Fig. S14). These results indicate that Mo is useful for protecting the  $\text{BiVO}_4$  semiconductor from photocorrosion, while the role of B doping is the modification with the catalytic local environment, facilitating seawater chlorination/oxidation. Besides, the Mo gradient doping into the BVO from the top surface, substituted  $\text{V}^{5+}$ , which acts as an electron donor in the lattice, boosts the charge separation and transfer, and reduces the surface recombination of electrode/electrolyte [16]. The Mott-Schottky measurement was utilized to explore the donor concentration of corresponding electrodes (Fig. S15). The low slopes of BVO and B/BVO have no visible change with reference to the Mo/BVO and MoB/BVO. It should be mentioned that the slope is inconsistent with the bulk homogeneous doping owing to the surface gradient doping (less than 50 nm). For example, a pronouncedly low slope is attained on Mo doped  $\text{BiVO}_4$  as reported by Zou et al. [16].

The surface integrity on the MoB/BVO electrode after 30 h of stability was analyzed. The surface becomes relatively smooth after long-term test from SEM and TEM observation Figs. S16 and S17 which may be assigned to the etching coming from the  $\text{Cl}^-$  ions in simulated seawater. Previous experience has shown that the fluorine ions from borate electrolyte could etch and passivate the surface of  $\text{BiVO}_4$ , avoiding the cocatalyst reconstruction and improving the photocorrosion resistance of  $\text{BiVO}_4$  [29]. XPS data denote the existence of Cl (1.90 at%), and in the interval, the Mo and B remain (4.65 at% and 1.37 at%) after the measurement. The Mo has some losses in comparison to the sample before durability (7.28 at%), whereas no noticeable change is found on B before and after stability (Fig. S18). To clarify the anti-photocorrosion resistance in seawater environment, the deposition layers (Mo, B, and MoB) were synthesized on the 304 stainless steel (304 SS) and measured the anti-corrosion ability in SSW as evident in Fig. 3c. Similarly, both MoB/304 SS and Mo/304 SS display significantly positive shifts of corrosion potentials located at 570–594 mV compared to the 304 SS (355 mV). Specifically, the Mo/304 SS shows the lowest corrosion potential, better than the MoB/304 SS (Table S2), along with 50 h of durability at open circuit potential (Fig. 3d). These results indicate the efficiently electrochemical anodic protection for corrosion protection of stainless steel and promising prospects on marine applications.

To further corroborate the beneficial influence on the modification of  $\text{MoO}_3$ , the natural seawater (SW) was used to examine the PEC activity and stability. Encouragingly, the MoB/BVO displays the resembled

photocurrent density in SW and SSW (inset of Fig. 3f). More importantly, the electrode presents a long durability of 70 h in SW (Fig. 3f). Note that the obviously fluctuated curve can be seen from the  $J$ - $t$  curve of MoB/BVO, manifesting the alternate occurrence of corrosion and passivation states. This phenomenon is also perceived for the electrode tested in simulated seawater (Fig. 3b). On the other hand, there is an increased photoresponse at the initial time, representing the passivated layer or the protected layer formed on the surface, which is consistent with the corrosion study [30]. In conjunction with the above, the active surface is present in the whole process, which leads to the relatively stable and efficient PEC performance. The increased PEC performance of MoB/BVO is assumed to the acceleration of the surface photogenerated carrier separation and the reduction of the electron-hole recombination at the surface made by B and Mo doping, therefore promoting an excellent stability and anti-corrosion protection in the ocean environment.

### 3.4. Impacts of surface Mo and B doping for PEC activity and stability

To further investigate the roles of Mo and B, the PEC performance and stability were evaluated in KBI electrolyte ( $\text{pH}=9.5$ ). As expected, the B/BVO has a visible enhancement in photocurrent compared to the Mo/BVO (Fig. 4a). The increased PEC performance on Mo/BVO is ascribed to the Mo doping approach to the top surface. However, all electrodes display the fast decay in photoresponse at  $1.23\text{ V}_{\text{RHE}}$  during the stability test (Fig. 4b), which completely differs from the results in seawater media (Fig. 3b). Further applying a relatively low potential of  $0.8\text{ V}_{\text{RHE}}$ , the Mo/BVO still shows a quickly decreased photocurrent, whereas the B/BVO and MoB/BVO have a better stability with a duration of 20–40 h (Fig. 4c), owing to the passivated surface state made by B. Additionally, there is an interesting phenomenon happened on the stability tests on the pristine BVO in SSW and KBI electrolytes. The BVO shows a slower decay rate in SSW (Fig. S14) than that of in KBI (Fig. S19). This can be ascribed to the fast oxidation of photogenerated holes by chloride ions in contrast to water, which leads to the relatively low photocorrosion rate. The  $\text{Cl}^-$  ions do not bring a bad influence on the seawater splitting system to some extent. Besides, these results again manifest that the  $\text{MoO}_3$  indeed does not act as the cocatalyst in the borate buffer solution.

On the other hand, a series of control experiments by the immersion approach was monitored with the same duration. Fig. 4d–i compares the PEC activity and stability characteristics of the optimized electrodes. Similar experimental results can be attained, and the Mo/BVO by the soaking approach still exhibits stable durability compared to the electrodeposition (Figs. S20 and S21). Conversely, the MoB/BVO has poor photoactivity and photostability under the same soaking condition. Except for the top modification of  $\text{MoO}_3$ , the surface near to the reaction becomes more important by electrodeposition, and the induced surface defects (e.g., doping) further reduce the surface charge recombination, which is one of the sparkling points in this work. This also demonstrates the cathodic electrodeposited method for benefiting from the modification of the surface structure. Two reaction processes happen in seawater splitting, where the chlorine ( $\text{Cl}_2$ ) is produced in the photoanode and the hydrogen ( $\text{H}_2$ ) is generated in the cathode. Little bubbles were detected on the MoB/BVO photoanode owing to the higher solubility of  $\text{Cl}_2$  in seawater than that of  $\text{H}_2$ . The dissolved  $\text{Cl}_2$  further reacts with water to form  $\text{HClO}$  and  $\text{Cl}^-$ . Thereby, the time-dependent productions of  $\text{HClO}$  from SSW on the electrode were investigated (Fig. 3 and S22). After 1 h of continuous operation, the amount of  $\text{Cl}_2$  produced from MoB/BVO photoanode is determined to be  $50\text{ }\mu\text{mol L}^{-1}$ .

### 3.5. DFT calculations for CER/OER and dissolving energy

The density functional theory (DFT) calculations were implemented to demonstrate the reaction pathways on the electrodes for CER, and to study the mechanism of the benefits from B and Mo doping. Since CER and OER will become competitive reactions taking part in the



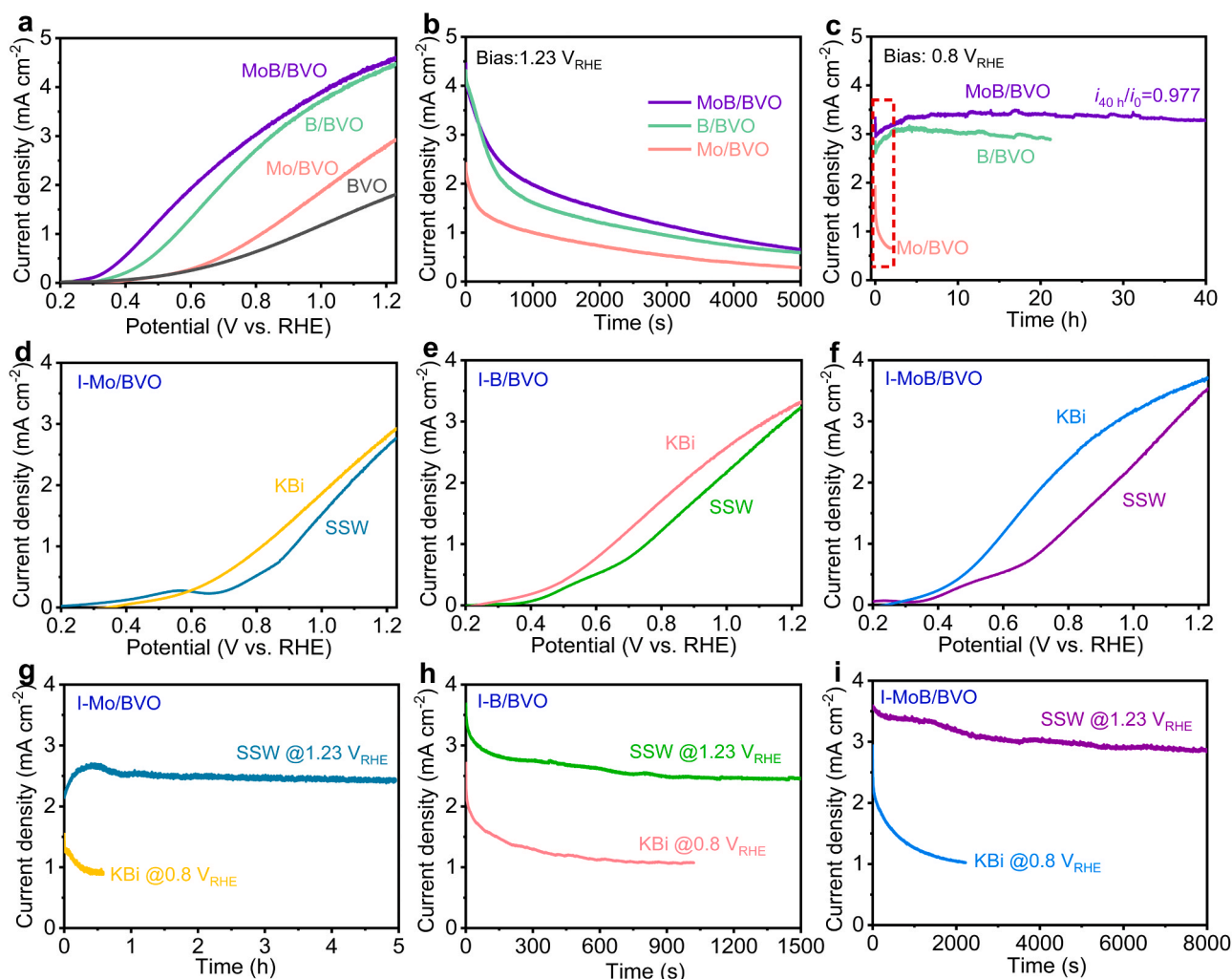


**Fig. 4.** (a) *J-V* curves of BVO, Mo/BVO, B/BVO, and MoB/BVO in KBI (pH = 9.5) under AM 1.5G front-side illumination; (b,c) *J-t* curves of corresponding electrodes applied at 1.23  $V_{RHE}$  (b) and 0.8  $V_{RHE}$  (c) in KBI under AM 1.5 G front-side illumination; (d-f) *J-V* curves of Mo/BVO, B/BVO, and MoB/BVO prepared by immersion approach in KBI (pH=9.5) and SSW electrolytes under AM 1.5G front-side illumination; (g-i) *J-t* curves of corresponding electrodes in 1 M KBI applied at 0.8  $V_{RHE}$  and SSW applied at 1.23  $V_{RHE}$  under AM 1.5G front-side illumination.

electrocatalysis, we firstly considered both reactions proposed by Nørskov et al. [31] As shown in Fig. 5a,b, the rate-determining step on BVO is the formation of  $\ast O$  from  $\ast OH$  ( $\ast OH \rightarrow \ast O + H^+ + e^-$ ) with  $\Delta G = -1.19$  eV, and that is the transformation of  $Cl_2$  from the  $\ast Cl$  and  $Cl^-$  ( $\ast Cl + Cl^- \rightarrow Cl_2(g) + e^-$ ) with  $\Delta G = -1.29$  eV. For the MoB/BVO the rate-determining step changes to be the formation of  $\ast OOH$  from  $\ast O$  ( $\ast O + H_2O \rightarrow \ast OOH + H^+ + e^-$ ) with  $\Delta G = -1.32$  eV, and that moves to the formation of  $Cl_2$  with  $\Delta G = -1.66$  eV. These results suggest that the evolution of  $Cl_2$  would be a favored process in comparison to the production of  $O_2$  on the MoB/BVO and BVO. Combined with the experimental results of various pH values of SSW (Fig. S23), the  $Cl_2$  from the BVO is still produced even as the pH of SSW was adjusted to high value (>9). The only difference is that the oxygen evolution reaction becomes the favored process at a high pH value, accompanied by the low generation of  $Cl_2$ .

Sequentially, the theoretical overpotentials of CER were plotted in Fig. 5c. The catalyst located closer to the volcano top will have a high electrocatalytic activity. It can be seen that the B/BVO and MoB/BVO exhibit a quick CER reaction with low overpotential ( $U_L$ ) values (0.10 V and 0.15 V) as compared to those of BVO (0.51 V) and Mo/BVO (0.59 V). The dual atoms doping would affect the reactive activity of Bi to some extent. In detail, Mo doping has a slight change on the oxophilicity of Bi, while after B doping, it greatly weakens the oxophilicity

of Bi, and makes the Cl adsorbed too strongly moves to the volcanic peak. Mo just plays a role in slightly tuning the adsorption energy. This is consistent with the experimental result, and the B/BVO has shown an enhanced PEC activity. Further, the dissolving energy of Mo and B on BVO was discussed as illustrated in Fig. 5d. The ability of dissolving energy is in the order of MoB/BVO > Mo/BVO > B/BVO > BVO, which manifests that the Mo and B provide the strong bond strength for protecting the BVO from corrosion. The calculated results provide an additionally strong evidence that the MoB/BVO has a better CER performance, compatible with the above experimental results.

#### 4. Conclusion

In summary, we for the first time report an ultra-stable PEC system for seawater splitting regarding Mo and B dual-doping  $BiVO_4$  protected by  $MoO_3$  barrier layer. The modified  $BiVO_4$  photoanode displays a resembled photocurrent density value of  $4.30 \text{ mA cm}^{-2}$  at 1.23  $V_{RHE}$  in simulated seawater and natural seawater under one sun AM 1.5G illumination. More importantly, the resulting photoanode shows a strong photocorrosion resistance character over 70 h in natural seawater splitting under irradiation. The enhanced PEC performance could be attributed to the deposition of  $MoO_3$  layer on the surface, accompanied with Mo and B gradually co-doping into the interface of  $BiVO_4$ .

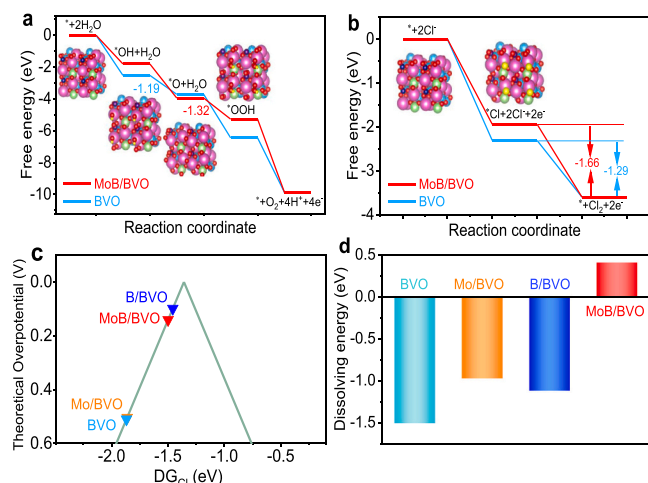


**Fig. 5.** (a,b) DFT calculation results of Gibbs free diagrams for (a) four elementary steps of OER and (b) two elementary steps of CER on BVO and MoB/BVO; (c) theoretical volcano plot of CER on BVO, Mo/BVO, B/BVO, and MoB/BVO. The left and right branches refer to catalysts that binds strongly and weakly to Cl<sup>-</sup> compared with the optimal adsorption; (d) dissolving energy of corresponding electrodes. Dissolving energy is the energy demanded to drag the associated atom from catalyst into solution. And it is calculated by the binding energy (BE, the energy needed to remove an atom from a compound) differences between the atoms in the two phases, which is  $E^{\text{dissolve}}(\text{A}) = \text{BE}(\text{A in solution}) - \text{BE}(\text{A in catalyst})$  for atom A. Note that in solution V, Mo and B exist as  $\text{NaVO}_3$ ,  $\text{NaMoO}_3$  and  $\text{Na}_3\text{BO}_3$ .

electrolyte, which reduces the substantial surface recombination and improve the (photo)corrosion resistance during long-term durability in the marine environment. This work provides a new avenue for designing robust and stable PEC semiconductors for hydrogen production by seawater photoelectrolysis.

#### CRediT authorship contribution statement

L.W. and R.-T.G. conceived the idea. R.-T.G. synthesized and characterized the materials. X.G., S.L., X.Z., X.L., and Y.S. assisted the data analysis and discussion. L.W. and R.-T.G. wrote the original manuscript. Y.S. and L.W. revised the manuscript. All authors contributed to the discussion and declare no conflict of interest.

#### Declaration of Competing Interest

The authors declare that they have no known competing financial interests or personal relationships that could have appeared to influence the work reported in this paper.

#### Acknowledgments

The authors acknowledge the financial support from the National Natural Science Foundations of China (51802320, 21872074, 21965024), the 111 project (D20033), the Central Government Guiding Special Funds for the Development of Local Science and Technology (2020ZY0012), the Natural Science Foundation of Inner Mongolia Autonomous Region of China (2020JQ01), Young science and technology talents cultivation project of Inner Mongolia University (21221505), start-up funding of Inner Mongolia University (10000-21311201/137),

and the opening project of Key Laboratory of Materials Processing and Mold from Zhengzhou University.

#### Appendix A. Supporting information

Supplementary data associated with this article can be found in the online version at doi:10.1016/j.apcatb.2021.120883.

#### References

- [1] J. Chang, G. Wang, Z. Yang, B. Li, Q. Wang, R. Kuliev, N. Orlovskaya, M. Gu, Y. Du, G. Wang, Y. Yang, *Adv. Mater.* 33 (2021) 2101425.
- [2] S. Drespf, F. Dionigi, M. Klingenhof, P. Strasser, *ACS Energy Lett.* 4 (2019) 933–942.
- [3] M. Jadowski, L. Jakubow-Piotrowska, P. Kedzierzawski, K. Bienkowski, J. Augustynski, *Adv. Energy Mater.* 10 (2020) 1903213.
- [4] S.-H. Hsu, J. Miao, L. Zhang, J. Gao, H. Wang, H. Tao, S.-F. Hung, A. Vasileff, S. Z. Qiao, B. Liu, *Adv. Mater.* 30 (2018) 1707261.
- [5] H. Jin, X. Wang, C. Tang, A. Vasileff, L. Li, A. Slattery, S.-Z. Qiao, *Adv. Mater.* 33 (2021) 2007508.
- [6] a) M. Sun, R.-T. Gao, J. He, X. Liu, T. Nakajima, X. Zhang, L. Wang, *Angew. Chem. Int. Ed.* 60 (2021) 17742–17748; b) S. Liu, J. Zhu, M. Sun, Z. Ma, K. Hu, T. Nakajima, X. Liu, P. Schmuki, L. Wang, *J. Mater. Chem. A* 8 (2020) 2490–2497; c) S. Liu, R.-T. Gao, M. Sun, Y. Wang, T. Nakajima, X. Liu, W. Zhang, L. Wang, *Appl. Catal. B* 292 (2021), 120063.
- [7] S. Ichikawa, *Int. J. Hydrogen Energy* 22 (1997) 675–678.
- [8] J.H. Kim, S.M. Hwang, I. Hwang, J. Han, J.H. Kim, Y.H. Jo, K. Seo, Y. Kim, J.S. Lee, *iScience* 19 (2019) 232–243.
- [9] Y. Li, R. Wang, H. Li, X. Wei, J. Feng, K. Liu, Y. Dang, A. Zhou, *J. Phys. Chem. C* 119 (2015) 20283–20292.
- [10] S. Kim, D.S. Han, H. Park, *Appl. Catal. B: Environ.* 284 (2021), 119745.
- [11] W. Zang, T. Sun, T. Yang, S. Xi, M. Waqar, Z. Kou, Z. Lyu, Y.P. Feng, J. Wang, S. J. Pennycook, *Adv. Mater.* 33 (2020) 2003846.
- [12] L. Yu, Q. Zhu, S. Song, B. McElhenny, D. Wang, C. Wu, Z. Qin, J. Bao, Y. Yu, S. Chen, Z. Ren, *Nat. Commun.* 10 (2019) 5106.
- [13] C. Ros, S. Murcia-Lopez, X. Garcia, M. Rosado, J. Arbiol, J. Llorca, J.R. Morante, *ChemSusChem* 14 (2021) 2872–2881.
- [14] J.S. Ko, J.K. Johnson, P.I. Johnson, Z. Xia, *ChemCatChem* 12 (2020) 4526–4532.
- [15] S. Trasatti, *Electrochim. Acta* 29 (1984) 1503–1512.
- [16] W. Luo, Z. Yang, Z. Li, J. Zhang, J. Liu, Z. Zhao, Z. Wang, S. Yan, T. Yu, Z. Zou, *Energy Environ. Sci.* 4 (2011) 4046–4051.
- [17] T.W. Kim, K.-S. Choi, *Science* 343 (2014) 990.
- [18] R.-T. Gao, X. Liu, X. Zhang, L. Wang, *Nano Energy* 89 (2021), 106360.
- [19] a) R.-T. Gao, D. He, L. Wu, K. Hu, X. Liu, Y. Su, L. Wang, *Angew. Chem. Int. Ed.* 59 (2020) 6213–6218; b) R.-T. Gao, L. Wang, *Angew. Chem. Int. Ed.* 59 (2020) 23094–23099; c) R.-T. Gao, S. Liu, X. Guo, R. Zhang, J. He, X. Liu, T. Nakajima, X. Zhang, L. Wang, *Adv. Energy Mater.* (2021), <https://doi.org/10.1002/aenm.202102384>.
- [20] B. Klahr, S. Gimenez, F. Fabregat-Santiago, J. Bisquert, T.W. Hamann, *Energy Environ. Sci.* 5 (2012) 7626–7636.
- [21] M. Zhang, H. Li, J. Chen, L. Yi, P. Shao, C.-Y. Xu, Z. Wen, *Chem. Eng. J.* 422 (2021), 130077.
- [22] P. Giannozzi, S. Baroni, N. Bonini, M. Calandra, R. Car, C. Cavazzoni, D. Ceresoli, G.L. Chiarotti, M. Cococcioni, I. Dabo, A.D. Corso, S. de Gironcoli, S. Fabris, G. Fratesi, R. Gebauer, U. Gerstmann, C. Gougousis, A. Kokalj, M. Lazzeri, L. Martin-Samos, N. Marzari, F. Mauri, R. Mazzarello, S. Paolini, A. Pasquarello, L. Paulatto, C. Sbraccia, S. Scandolo, G. Sclauzero, A.P. Seitsonen, A. Smogunov, P. Umari, R.M. Wentzcovitch, *J. Phys. Condens. Matter* 21 (2009), 395502.
- [23] H. Chen, J. Li, W. Yang, S.E. Balaghi, C.A. Triana, C.K. Mavrokefalos, G.R. Patzke, *ACS Catal.* 11 (2021) 7637–7646.
- [24] Q. Shi, S. Murcia-Lopez, P. Tang, C. Flox, J.R. Morante, Z. Bian, H. Wang, T. Andreu, *ACS Catal.* 8 (2018) 3331–3342.
- [25] Q. Meng, B. Zhang, L. Fan, H. Liu, M. Valvo, K. Edstrom, M. C. uartero, R. de Marco, G.A. Crespo, L. Sun, *Angew. Chem. Int. Ed.* 58 (2019) 19027–19033.
- [26] Q. Meng, B. Zhang, H. Yang, C. Liu, Y. Li, A. Kravchenko, X. Sheng, L. Fan, F. Li, L. Sun, *Mater. Adv.* 2 (2021) 4323–4332.
- [27] Y. Wu, H. Wang, W. Tu, S. Wu, J.W. Chew, *Appl. Organo Chem.* 33 (2019) 4780.
- [28] H. Zhang, W. Wu, Q. Liu, F. Yang, X. Shi, X. Liu, M. Yu, X. Lu, *Angew. Chem. Int. Ed.* 60 (2021) 896–903.
- [29] R.-T. Gao, L. Wu, S. Liu, K. Hu, X. Liu, J. Zhang, L. Wang, *J. Mater. Chem. A* 9 (2021) 6298–6305.
- [30] L. Wang, T. Shinohara, B.-P. Zhang, *J. Alloy Compd.* 496 (2010) 500–507.
- [31] J.K. Nørskov, J. Rossmeisl, A. Logadottir, L. Lindqvist, J.R. Kitchin, T. Bligaard, H. Jonsson, *J. Phys. Chem. B* 108 (2004) 17886–17892.